

ter will be determined from an analysis of the IRIS radiometer data.

Triton. Triton is an extremely cold object. Few individual IRIS spectra appear to show any thermal signature at all. An average of 16 spectra from the dayside hemisphere (average solar incidence angle, 36°) is shown in Fig. 8A. The spectrum is dominated by noise; nonetheless there appears to be a small signal from Triton at low wavenumbers, an impression corroborated by fitting a Planck function to the spectrum by least squares. The fit was restricted to the region between 200 and 350 cm^{-1} , beyond which little or no signal is expected. The spectral data were weighted inversely as the square of the instrument noise equivalent spectral radiance (NESR) to account for the wavenumber dependence of the noise. The best fit temperature (corresponding to a surface with unit emissivity) is 38 K. Figure 8B shows the residual of the fit, plotted within the noise envelope expected from the NESR; the behavior of the residual appears random. Estimated upper and lower bounds, somewhat arbitrarily defined as the temperatures that result in an increase of 5% in the RMS residual of the fits, are 41 and 34 K, respectively. Planck curves for all of these temperatures are shown in Fig. 8A. For a surface with an emissivity of 0.5 in the spectral region of the fit, the temperature estimate is $T_s = 41^{+3}_-5$ K. Temperatures in this range (34 to 41 K) correspond to surfaces with Bond albedos of $A > 0.8$, consistent with the location of the present observations on Triton's bright polar region.

As a result of ground-based measurements, CH_4 and N_2 have been identified on the surface of Triton (25). Additionally, both species have been identified in the atmosphere from Voyager Ultraviolet Spectrometer data (26). The 38 K surface temperature derived here lies in the β regions of solid CH_4 and N_2 (27). From vapor pressure curves for these phases (28), equilibrium atmospheres over pure CH_4 and N_2 would have surface pressures of approximately 2×10^{-9} and 20×10^{-6} bars, respectively; the stated temperature limits permit more than an order of magnitude uncertainty in each of these pressure estimates. If any significant amount of solid N_2 is present, however, CH_4 can only be a minor constituent of the atmosphere. Additional effects, such as the presence of solid solutions, mass flow of the atmosphere, and cold trapping, will tend to alter the actual surface pressure from these ideal values.

REFERENCES AND NOTES

1. R. Hanel *et al.*, *Appl. Opt.* **19**, 1391 (1980).
2. R. Hanel *et al.*, *Science* **204**, 972 (1979).
3. R. Hanel *et al.*, *ibid.* **206**, 952 (1979).

4. R. Hanel *et al.*, *ibid.* **212**, 192 (1981).
5. R. Hanel *et al.*, *ibid.* **215**, 544 (1982).
6. R. Hanel *et al.*, *ibid.* **233**, 70 (1986).
- 6a. The stratosphere denotes that portion of the atmosphere where temperature increases with altitude (that is, with decreasing barometric pressure) above the temperature minimum, or tropopause, near 200 mbar (Fig. 3). The troposphere denotes the atmosphere below the tropopause where temperature decreases with altitude.
7. D. Gautier *et al.*, *J. Geophys. Res.* **86**, 8713 (1981); B. Conrath, D. Gautier, R. Hanel, J. Hornstein, *Astrophys. J.* **282**, 807 (1984); B. Conrath, D. Gautier, R. Hanel, G. Lindal, A. Marten, *J. Geophys. Res.* **92**, 15,003 (1987).
8. D. Gautier, *Philos. Trans. R. Soc. London Ser. A* **325**, 583 (1988).
9. W. Macy and W. Sinton, *Astrophys. J.* **218**, L79 (1977).
10. G. S. Orton, A. T. Tokunaga, J. Caldwell, *Icarus* **56**, 147 (1983).
11. G. S. Orton *et al.*, *ibid.* **70**, 1 (1987).
12. G. S. Orton *et al.*, *ibid.*, in press.
13. P. N. Romani and S. K. Atreya, *ibid.* **74**, 442 (1988).
14. ———, *Geophys. Res. Lett.* **16**, 941 (1989).
15. B. J. Conrath and D. Gautier, in *Remote Sensing of Atmospheres and Oceans*, A. Deepak, Ed. (Academic Press, New York, 1980), p. 611.
16. F. M. Flasar, B. J. Conrath, P. J. Gierasch, J. A. Pirraglia, *J. Geophys. Res.* **92**, 15,011 (1987).
17. B. A. Smith *et al.*, *Science* **246**, 1422 (1989); H. B. Hammel *et al.*, *ibid.* **245**, 1367 (1989).
18. F. M. Flasar *et al.*, *J. Geophys. Res.* **86**, 8759 (1981).
19. J. R. Holton, *An Introduction to Dynamic Meteorology* (Academic Press, New York, 1979).
20. B. J. Conrath and J. A. Pirraglia, *Icarus* **53**, 286 (1983).
21. P. J. Gierasch, B. J. Conrath, J. A. Magalhaes, *ibid.* **67**, 456 (1986).
22. B. J. Conrath, P. J. Gierasch, S. S. Leroy, *ibid.*, in press; B. Bezard, *Adv. Space Res.*, in press.
23. G. Orton *et al.*, *Bull. Am. Astron. Soc.* **17**, 745 (1985).
24. J. B. Pollack *et al.*, *Icarus* **65**, 424 (1986).
25. D. P. Cruikshank and P. M. Silvaggio, *Astrophys. J.* **233**, 1016 (1979); J. Apt, N. P. Carleton, C. D. Mackay, *ibid.* **270**, 342 (1983); D. P. Cruikshank and J. Apt, *Icarus* **58**, 306 (1984); D. P. Cruikshank, R. H. Brown, R. N. Clark, *ibid.*, p. 293; D. P. Cruikshank, R. H. Brown, L. P. Giver, A. T. Tokunaga, *Science* **245**, 283 (1989).
26. A. L. Broadfoot *et al.*, *Science* **246**, 1459 (1989).
27. A. I. Prokhatilov and L. D. Yantsevich, *Sov. J. Low Temp. Phys.* **9**, 94 (1983).
28. G. N. Brown and W. T. Ziegler, *Adv. Cryog. Eng.* **25**, 662 (1980).
29. We thank A. L. Lane for making computing facilities available to us at the Jet Propulsion Laboratory, J. Piotrowski and W. Smythe for computer system assistance, M. Reisdorf for logistic support, and the Voyager Project staff for their continued support of this investigation. We also thank those at Goddard Space Flight Center who have assisted with data processing, particularly J. Guerber, L. Herath, L. Mayo, M. Silverstein, C. Staub, and J. Tingley.

1 November 1989; accepted 15 November 1989

Ultraviolet Spectrometer Observations of Neptune and Triton

A. L. BROADFOOT, S. K. ATREYA, J. L. BERTAUX, J. E. BLAMONT, A. J. DESSLER, T. M. DONAHUE, W. T. FORRESTER, D. T. HALL, F. HERBERT, J. B. HOLBERG, D. M. HUNTEN, V. A. KRASNOPOLSKY, S. LINICK, J. I. LUNINE, J. C. MCCONNELL, H. W. MOOS, B. R. SANDEL, N. M. SCHNEIDER, D. E. SHEMANSKY, G. R. SMITH, D. F. STROBEL, R. V. YELLE

Results from the occultation of the sun by Neptune imply a temperature of 750 ± 150 kelvins in the upper levels of the atmosphere (composed mostly of atomic and molecular hydrogen) and define the distributions of methane, acetylene, and ethane at lower levels. The ultraviolet spectrum of the sunlit atmosphere of Neptune resembles the spectra of the Jupiter, Saturn, and Uranus atmospheres in that it is dominated by the emissions of H Lyman α (340 ± 20 rayleighs) and molecular hydrogen. The extreme ultraviolet emissions in the range from 800 to 1100 angstroms at the four planets visited by Voyager scale approximately as the inverse square of their heliocentric distances. Weak auroral emissions have been tentatively identified on the night side of Neptune. Airglow and occultation observations of Triton's atmosphere show that it is composed mainly of molecular nitrogen, with a trace of methane near the surface. The temperature of Triton's upper atmosphere is 95 ± 5 kelvins, and the surface pressure is roughly 14 microbars.

BEFORE THE VOYAGER ENCOUNTER, neither Neptune nor Triton had been detected at wavelengths shorter than 1700 Å. Measurements of the ultraviolet (UV) reflection spectrum and the infrared (IR) spectrum of Neptune gave contradictory implications about the distribution of methane (CH_4), ethane (C_2H_6), and acetylene (C_2H_2) in the stratosphere. A tem-

perature of 150 K at the 1- μ bar level had been deduced from observations of a stellar occultation. A 1σ upper limit on H Lyman α as low as 180 R ($1\text{ R} = 10^{10}/4\pi$ photons $\text{m}^{-2}\text{ s}^{-1}\text{ sr}^{-1}$) above the background emission was derived from International Ultraviolet Explorer (IUE) observations. Features in Triton's IR reflection spectrum were interpreted as indicating the presence of CH_4

and N₂ frosts on the surface, which, in turn, suggested the presence of a N₂-CH₄ atmosphere (1). Atmospheric emissions are so subdued and so distant that nearby sensing, such as made possible by Voyager, is the best present means of determining the composition and structure of the atmospheres of Neptune and Triton. Moreover, Neptune's magnetosphere is so quiescent that long exposures from short range are required to yield indications of auroral emissions. The Ultraviolet Spectrometer (UVS) (2) is well suited to make such measurements, and we present here our initial report.

Neptune's atmosphere, thermal structure, and vertical mixing. We measured the transmission of Neptune's atmosphere by recording the solar spectrum during the atmospheric occultation. The geometrical characteristics of this occultation, and occultations of the sun and a star by Triton, are summarized in Table 1. Figure 1 shows light curves from the entrance solar occultation for several key wavelength λ regions (3). Continuum absorption by H₂ at wavelengths <845 Å (Fig. 1A) probes the highest levels in the atmosphere (pressure $p \sim 10^{-5}$ μ bar). Absorption in the discrete transitions of the H₂ electronic band systems begins to be detectable near 1200 km and extends downward to 400 km (Fig. 1B). The abrupt drop in transmission near 400 km ($p \sim 0.03$ μ bar) (Fig. 1C) is due to CH₄ absorption. Extinction in the region from 1570 to 1634 Å (Fig. 1D) begins near 50 km, where we estimate the pressure to be 100 μ bar. This extinction has been tentatively ascribed to Rayleigh scattering in H₂. Other molecules also absorb in this region, notably C₂H₂, but the lack of absorption features at other wavelengths appears to rule it out as the dominant absorber. In total, the occultation has probed Neptune's atmosphere over an altitude range of ~ 2000 km, corresponding to approximately seven decades in pressure.

The model curves compared to the data in

Table 1. UVS occultation observations.

Star/body	Latitude, longitude	Resolution (km)	Time relative to encounter (hours)	Notes
Sun/Neptune	61°N, 259°W	5	+0.1	Entrance
Sun/Neptune	49°S, 160°W	15	+0.9	Exit
Sun/Triton	26°N, 305°W	9	+5.7	Entrance
Sun/Triton	44°S, 180°W	9	+5.7	Exit
β Canis Majoris/Triton	20°S, 339°W	6	+5.2	Entrance
β Canis Majoris/Triton	3°N, 173°W	6	+5.2	Exit
σ Sagittarii/rings		2	-4.5	3.1 to 1.7 R_N

Fig. 1 were computed from the model atmosphere shown in Fig. 2. From the H₂ continuum absorption we derive a temperature of 750 K at altitudes above about 2000 km, which is very close to the value on Uranus. (Here we use a radius of 24,600 km for our distance above the surface $z = 0$ reference at this 66°N occultation, corresponding roughly to last light. The pressure at $z = 0$ is ~ 200 μ bar.) However, data-processing issues remain to be resolved before we obtain a definitive value for the exospheric temperature, and the value of 750 ± 150 K (the error limits in the text, tables, and figures are $\pm 1\sigma$ limits) should be regarded as provisional. From the H₂ Rayleigh scattering extinction we derive a temperature of 150 K in the region from 1 to 100 μ bar, which is consistent with the results from ground-based stellar occultations. The H₂ band data indicate a temperature near 250 K in the 10^{-2} - μ bar region. To these separate measurements we have applied the additional constraint of hydrostatic equilibrium to obtain the model atmosphere shown in Fig. 2. The break in slope of the temperature profile near 2000 km (10^{-5} μ bar) is a signature of energy deposition. We estimate that a heat-

ing rate of ~ 0.1 erg cm⁻² s⁻¹ at this level is required to produce the 750 K exospheric temperature.

The abundance of atomic hydrogen is best inferred from absorption at wavelengths between 845 and 912 Å, where H absorbs in its ionization continuum, and at H Lyman α (1216 Å). The H₂ profile is used to correct for discrete H₂ absorption in the former region. We derive an H density of about 5×10^8 cm⁻³ at an altitude of 500 km. On Uranus the extended H distribution and associated gas drag play important roles in ring evolution. Although the H densities and exospheric temperatures on Neptune are similar to those on Uranus, gas drag is weaker because of Neptune's larger mass, cold lower atmosphere, and larger ring system (4).

The CH₄ mole fraction deduced from the light curve in Fig. 1C is about 3×10^{-5} , which is well above the upper limit of 10^{-7} deduced at Uranus (3), indicating a significant difference between eddy mixing, CH₄ abundance, or both for these two planets. Because the apparent CH₄ scale height is intermediate between those expected for a completely mixed and for a diffusively sepa-

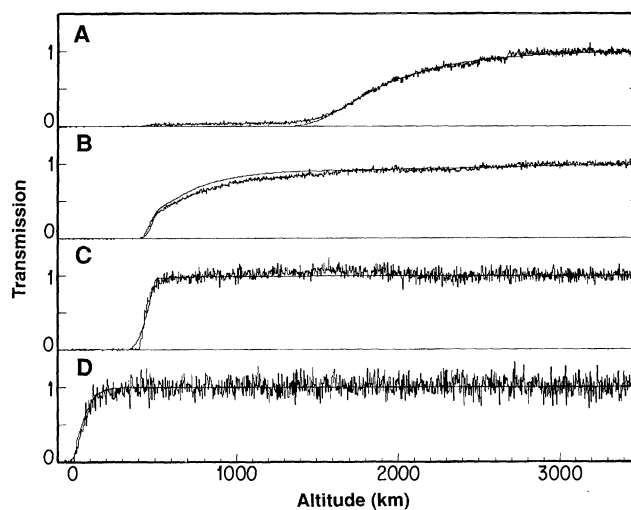


Fig. 1. Comparison of observed and model atmospheric transmission for the solar entrance occultation of Neptune. (A) Opacity due to the H₂ ionization continuum ($773 < \lambda < 838$ Å), from which the exospheric temperature is derived. Some uncompensated scattered light remains below 1400 km. (B) Opacity due to the Lyman and Werner bands of H₂ ($912 < \lambda < 1023$ Å). (C) Opacity due to the continuum absorption of CH₄ ($1106 < \lambda < 1189$ Å). The model follows the diffusive separation profile (scale height ≈ 12 km) in the upper part and a mixed profile (with

the dominant H₂ species, which has a scale height of about 95 km here) in the lower part of the curve. The observed scale height is intermediate between these two. (D) Opacity due to Rayleigh scattering in H₂ ($1570 < \lambda < 1634$ Å). The pressure at the bottom of this range is somewhat above 0.1 mbar. Note that the H₂ scale height in (D) is greater than the CH₄ scale height in (C).

A. L. Broadfoot, W. T. Forrester, D. T. Hall, F. Herbert, J. B. Holberg, D. M. Hunten, J. I. Lunine, B. R. Sandel, N. M. Schneider, D. E. Shemansky, R. V. Yelle, University of Arizona Lunar and Planetary Laboratory, Tucson, AZ 85721.

H. W. Moos and D. F. Strobel, Johns Hopkins University, Baltimore, MD 21218.

S. K. Atreya and T. M. Donahue, Department of Atmospheric and Oceanic Science, University of Michigan, Ann Arbor, MI 48109.

J. L. Bertaux and J. E. Blamont, Service d'Aeronomie du CNRS, 91370 Verrieres-le-Buisson, France.

J. C. McConnell, Department of Earth and Atmospheric Sciences, York University, Downsview, Ontario, Canada M3J 1P3.

A. J. Dessler, Department of Space Physics and Astronomy, Rice University, Houston, TX 77251.

G. R. Smith, Northwest College, Powell, WY 82435.

V. A. Krasnopolsky, Space Research Institute, 117810 Moscow, U.S.S.R.

S. Linick, Jet Propulsion Laboratory, California Institute of Technology, Pasadena, CA 91109.

Table 2. Emission features from Uranus and Neptune.

Transition	λ (\AA)	Intensity	
		Uranus	Neptune
HeI($1S \leftarrow 1P$)	584	<0.2 R	0.5 \pm 0.2 R
HI($2S \leftarrow 2P^0$) day	1216	1500 R	340 \pm 20 R
HI($2S \leftarrow 2P^0$) night	1216	170 R	85 \pm 5 R
H ₂ Lyman, Werner, Rydberg bands + HI($1s\ 2S \leftarrow np\ 2P^0$)	800–1100	46 R	19 \pm 3 R
Rayleigh-scattered sunlight	1290–1480	0.4 R/ \AA	0.07 \pm 0.04 R/ \AA
Rayleigh-scattered sunlight	1550–1600	8.8 R/ \AA	3.4 \pm 0.4 R/ \AA

rated atmosphere, either the homopause is near the 400- to 500-km level (0.01 to 0.1 μbar) or photochemistry is altering the distribution there, or (possibly) both. If the homopause is in this range (where $10^{11} < n_{\text{H}_2} < 10^{12} \text{ cm}^{-3}$, n is the number density), then the eddy diffusion coefficient there is near 10^7 to $10^8 \text{ cm}^2 \text{ s}^{-1}$. The absorption signatures of C_2H_2 and C_2H_6 are discernible at slightly lower altitudes, particularly in the variation of the shape of the absorption spectra with altitude. Preliminary values of the mixing ratios of C_2H_2 and C_2H_6 at 300 to 400 km (0.1 to 0.3 μbar) are approximately 2×10^{-7} and 3×10^{-5} , within about half an order of magnitude.

The albedo of the atmosphere in the wavelength range from 1550 to 1700 \AA can be used to derive an independent estimate of the C_2H_2 abundance in the lower stratosphere. The measured intensity of reflected sunlight in this wavelength range is $3.4 \pm 0.4 \text{ R}/\text{\AA}$. Scattering calculations for a Rayleigh-Raman atmosphere having a uniform distribution of C_2H_2 require a mixing ratio of 2×10^{-8} to produce this intensity. Although this model atmosphere is uniformly mixed, the geometric albedo is most sensitive to the C_2H_2 abundance near the $\tau = 1$ level (τ is optical depth), which is located at 10 mbar. The mixing ratio derived here is smaller than the value inferred in the upper stratosphere (the 0.01- to 2-mbar region) by Conrath *et al.* (5). We infer a steep gradient in C_2H_2 between 0.01 and 10 mbar. The C_2H_2 profile inferred from the UV albedo, occultation, and IR spectrum determinations is consistent with expectations based on the photochemical models of Romani and Atreya (6) and a value of the eddy diffusion coefficient at the homopause of $K_h \sim 3 \times 10^7 \text{ cm}^2 \text{ s}^{-1}$. In this model, the gradient between the 0.01- and 10-mbar levels is caused by coupled photochemical-cloud microphysical processes. The higher value of K_h at Neptune than at Uranus (3, 7) indicates more vigorous mixing of the atmosphere, which may be related to the larger internal heat source at Neptune.

Airglow from Neptune. Figure 3 shows the extreme ultraviolet (EUV) spectra of Nep-

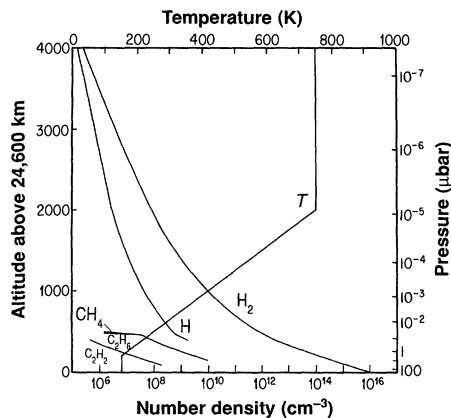


Fig. 2. Model Neptune atmosphere used to compute the transmission profiles that are compared with the measurements in Fig. 1. This is a provisional model of the atmosphere above a radius of 24,600 km at 66°N, where the entrance solar occultation occurred. The curves identified by chemical symbols indicate number densities. Helium is not shown because the UVS cannot detect it in absorption.

tune and Uranus. The Neptune spectrum is a sum of many observations carried out during the latitude-mapping sequence. Spectra obtained only when the planet filled the UVS slit are included, so the composite spectrum can be viewed as a latitudinal average over the subspacecraft meridian. The measured intensities in a number of wavelength bands are listed in Table 2. For comparison, intensities measured at Uranus are also shown. The brightness in the bands from 800 to 1100 \AA and 1550 to 1600 \AA is smaller on Neptune than on Uranus by a factor of approximately $2.5 = (30.2/19.1)^2$. The heliocentric scaling in the region from 800 to 1100 \AA continues a trend observed on Jupiter, Saturn, and Uranus (8), but the reason for the correlation is not yet understood (9). The H Lyman α intensity and the intensity in the region from 1290 to 1480 \AA are far below the values obtained by heliocentric scaling from Uranus.

The weak intensity in the spectral region between H Lyman α and 1500 \AA on Neptune relative to Uranus is probably a result of differences in the atmospheric structure. On Uranus, these emissions were originally interpreted as evidence for excitation of H_2

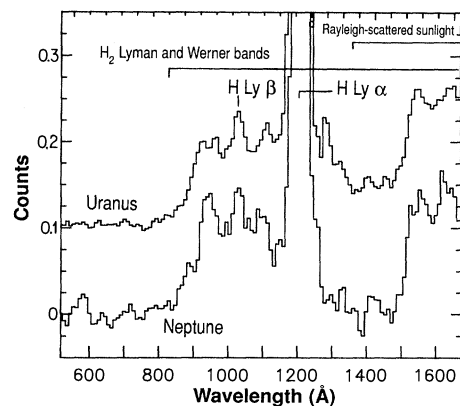


Fig. 3. The EUV spectrum of Neptune obtained 1 day before closest approach. The spectrum is an average over the subspacecraft meridian with the center of the UVS slit confined to distances of $\pm 0.5 R_N$ from planet center. A subsolar spectrum of Uranus, scaled by the inverse square of the ratio of the heliocentric distances and offset by 0.1 count, is shown for comparison.

by a gas of 3 eV-electrons, but more recently Yelle *et al.* (7, 8, 10) have argued that the emissions are probably caused by Rayleigh scattering of sunlight. If the latter interpretation is correct, the absence of these emissions on Neptune implies larger stratospheric CH_4 abundances than on Uranus, consistent with the occultation results. The relatively weak H Lyman α brightness of Neptune is also consistent with this interpretation. On Uranus, Rayleigh scattering of solar H Lyman α is believed to contribute 350 to 580 R of the observed 1500 R (7). If the CH_4 is distributed to higher altitudes on Neptune than on Uranus, the Rayleigh scattering component will be absent, leading to a lower H Lyman α brightness.

Figure 4 shows the intensity in three wavelength bands as a function of distance from the center of the disk. In this sequence, the slit was roughly half filled, so some of the variations near the edges of the planet are caused by changes in the slit-filling factor rather than by intrinsic brightness variations. The H_2 emission morphology in Fig. 4B is qualitatively reminiscent of that on Jupiter, Saturn, and Uranus in that the brightness appears correlated with the solar zenith angle (8).

As with Jupiter, Saturn, and Uranus, the H_2 band emissions vanish on the shadowed areas of Neptune, where we estimate an upper limit of 3 R on the integrated intensity in the 800- to 1100- \AA band. The H Lyman α intensity on the dark side is 85 R over most of the disk. The absence of H_2 band emissions on the dark side of the planet suggests a connection with solar excitation. Yelle *et al.* (8, 11) have argued that the emissions are produced by fluorescence of solar radiation. Using measured values

for the solar flux at the last solar maximum (12), we calculate that an H_2 column density of the order of 10^{21} cm^{-2} is required to produce the intensity observed in the region from 800 to 1100 Å. From the occultation results, we derive a similar H_2 column abundance above the $\tau = 1$ level in the absorbing CH_4 .

The apparent H Lyman α intensity (Fig. 4C) varies remarkably little during this sequence. The explanation involves the H Lyman α emissions from the Local Interstellar Medium (LISM), which are also observed by the UVS. Before encounter, the LISM intensity in Neptune's background was approximately 340 R. The intensity around $\pm 2 R_N$ (R_N is the Neptune radius)

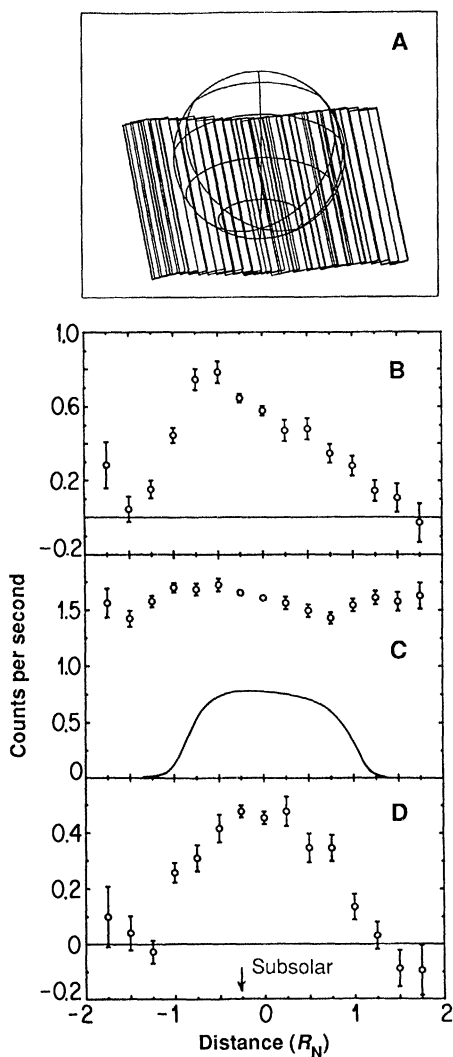


Fig. 4. Intensity in three wavelength bands as a function of distance from the center of the disk, measured parallel to the equatorial plane. The drawing (A) is representative of the scans that produced these data. Panels (B, C, and D) show, respectively, the wavelength regions 857 to 1115 Å, 1170 to 1255 Å, and 1475 to 1670 Å. The dominant contributors are indicated. The curve in (C) shows the fraction of the slit filled by Neptune.

in Fig. 4C is entirely from these LISM emissions, whereas the intensity near $0 R_N$ is predominantly from the planet. The constant intensity during this sequence means that the planetary brightness is nearly equal to the LISM brightness. We estimate that the disk-integrated brightness of Neptune is within $\pm 5\%$ of the LISM intensity. Moreover, through examination of the appropriate slit-filling factors, we estimate that the center-to-limb planetary H Lyman α emissions vary by less than 25% for the UVS viewing geometry.

The emission rate of the He resonance line at 584 Å is $0.5 \pm 0.2 R$ (1σ) on the day side and less than 0.2 R on the night side. The day-side intensity is a latitudinal average obtained over a period of about 4 hours. To be detectable at this wavelength, He atoms must be above most of the absorbing H_2 . Because diffusive separation tends to suppress the He concentration in the upper atmosphere, the He 584 Å brightness depends on the rate of vertical mixing, expressed by K_h . It also depends on the planetary He abundance and the temperature. Emission rates of the order of 0.5 R can be explained by resonance scattering of the solar 584 Å line with K_h in the range 10^7 to $10^8 \text{ cm}^2 \text{ s}^{-1}$, a He mole fraction of 15%, and a temperature of 400 K, appropriate for a height of 1000 km in Fig. 2. This value of K_h is consistent with the value derived from the hydrocarbon distributions. Similar values have been derived for Saturn and Jupiter, but at Uranus K_h is smaller by at least three orders of magnitude (13).

Neptune aurora. We tentatively identify faint aurora from the dark side of Neptune at longitudes $\sim 30^\circ$ and $200^\circ W$ (see Fig. 5). The auroral spectrum includes emission at the wavelength of H Lyman β (1025 Å) and an approximately equal contribution from a feature at slightly longer wavelength. There is no evidence for a corresponding auroral enhancement of H Lyman α . We propose that each aurora is driven by a partial plasma torus (a plasma arc) formed by gas escaping from Triton's atmosphere and becoming ionized preferentially at crossings of the plasma equator, as illustrated in Fig. 6. The plasma thus created settles to the plasma equator (at a latitude between the magnetic and centrifugal equators) and $L = 14$ to $16 R_N$. (A field line's L value is the distance from its magnetic equator crossing to the magnetic dipole.) The outward centrifugal stress on each of the plasma arcs creates a partial ring current wherein the $J \times B$ force balances the centrifugal force. The current $J = 2 \times 10^5 \text{ A}$ (14) is large enough to create instabilities that can drive auroral acceleration processes. This current closes through the ionosphere, in upward and downward

currents, corresponding to electron and ion bombardment near the connected magnetic poles. The aurora radiate $5 \times 10^7 \text{ W}$, so the plasma arcs must generate ~ 30 times that (or $\sim 10^9 \text{ W}$) to allow for conversion losses (15). The auroral detection is marginal, but we are encouraged by the concurrence between observation and a simple theory.

Triton's atmosphere. Before the Voyager flyby, the nature of Triton's atmosphere could only be inferred from the presence of CH_4 and N_2 frosts. It is now clear that there is an extended atmosphere, with interesting resemblances to Pluto and Titan. Airglow and occultation measurements show that the major gas is N_2 , at temperatures varying between 38 K near the surface to 95 K in the exosphere. Methane, though clearly present, is much less abundant than on either Titan or Pluto. Such differences are probably due to the remarkably low surface temperature, which stems from the high albedo.

The combination of exceedingly low temperature and pressure gives Triton's atmosphere an unusual thermal structure. The atmosphere does not have IR-active molecules in any significant concentration; consequently, radiative processes are negligible.

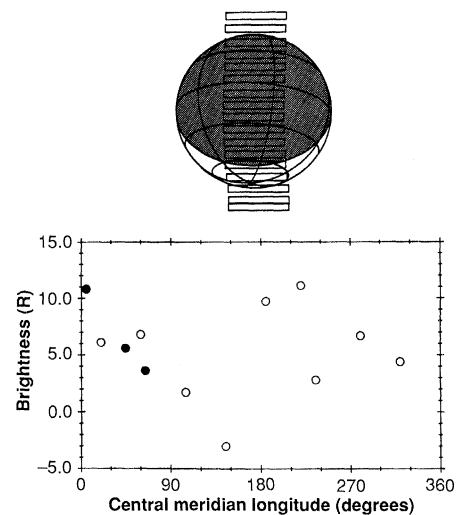


Fig. 5. Neptune dark-side emission versus the longitude of the central meridian as seen by Voyager. Integrated emission in the range $967 \leq \lambda \leq 1115 \text{ Å}$ from 12 successive observations of the nonilluminated portion of Neptune are plotted as a function of longitude (computed for a period of 16.06 hours). The filled points are from the beginning of a second rotation, which reproduces the enhancement that we place at $\sim 30^\circ W$. The observations consist of repeated north-south scans as shown in the drawing. The data were selected to avoid the illuminated crescent and bright sky background. Binning the same dark-side data into three latitude ranges yields separate intensity variations similar to these data except that the peak at 0 to $60^\circ W$ is relatively stronger in the north and the peak at $\sim 200^\circ W$ is stronger in the south, in rough agreement with the orientation of the magnetic dipole moment (30).

Rather, the thermal structure of the upper atmosphere is determined by thermal conduction, whereas convection and the release of latent heat should dominate the heat budget near the surface. Convection in the lower atmosphere may be driven by the seasonal transport of volatiles, primarily N_2 , the dominant atmospheric constituent. This joining of conductive (thermospheric) and convective (tropospheric) regions without an intervening radiative layer (that is, a stratosphere) is unique in the solar system. Triton presents us with a new type of atmosphere that will require extensive investigation to be properly understood. Here we report on the beginnings of these investigations.

Triton's EUV spectrum. The EUV spectrum of Triton shown in Fig. 7 suggests that the atmosphere is composed primarily of N_2 . The electronic transitions of N_2 in the c'_4 $^1\Sigma_u^+ - X$ $^1\Sigma_g^+$, c_3 $^1\Pi_u - X$ $^1\Sigma_g^+$, c_4 $^1\Pi_u - X$ $^1\Sigma_g^+$, and b $^1\Pi_u - X$ $^1\Sigma_g^+$ systems are consistent with the broad peak observed near 970 Å. NI and NII emissions also contribute to the spectrum. Although the spectral resolution is inadequate to identify individual emission features, we believe that the spectrum is clearly due to emissions from nitrogen. Other potential candidates such as carbon monoxide (CO), Ar, and Ne are inconsistent with the data. The emission spectrum of CO includes features in the region from 1467 to 1485 Å due to 5-2 and 2-0 bands of the Fourth Positive system, which are not observed. We estimate an upper limit of 9% on the CO abundance by this means, but a more stringent limit, based on the occultation results, is derived below. Argon should produce a strong resonance line at 1048 Å, which does not appear in the observed spectrum. Finally, the Ne line at 736 Å is not observed, implying an upper limit of 1%. The bright H Lyman α line implies the presence of atomic H in Triton's atmosphere, which is produced by CH_4 photochemistry, as on Titan and the outer planets. Some features at longer wavelengths are consistent with the positions of carbon lines at 1335, 1561, and 1657 Å. These features, if real, could result from scattering of solar lines by the atmosphere or surface and do not imply the presence of atomic carbon in the atmosphere. Table 3 gives the brightness of selected features in the Triton spectrum in comparison to those in the Titan spectrum.

Analysis of the Triton spectrum is hampered by the weak signal and high background. The detector background, which has been subtracted in Fig. 7, is caused mainly by magnetospheric particles. At the time of the observations this background was large and variable; therefore, the zero

Table 3. Emission features from Triton and Titan.

Transition	λ (Å)	Intensity (R)	
		Titan	Triton
N_2 c'_4 $^1\Sigma_u^+ \rightarrow X$ $^1\Sigma_g^+$ (0,0)	958	12	~0
N_2 c'_4 $^1\Sigma_u^+ \rightarrow X$ $^1\Sigma_g^+$ (0,1)	981	8.6	3-5
NII ($^3P \leftarrow ^3D^0$)	1085	12	2-8
HI ($^2S \leftarrow ^2P^0$) day	1216	700	110
HI ($^2S \leftarrow ^2P^0$) night	1216	300	<90

level of the spectrum is not well determined and the structure below 850 Å may be the result of uncertainties in the background subtraction.

So far, EUV emissions from Triton have been detected only from the sunlit atmosphere. The emissions on the night side are

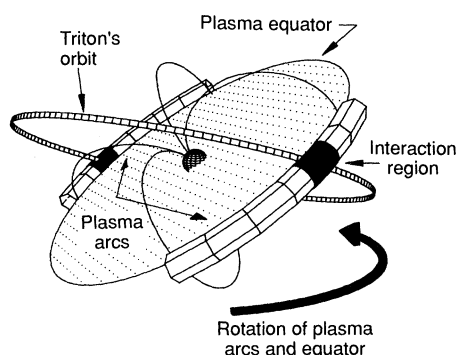
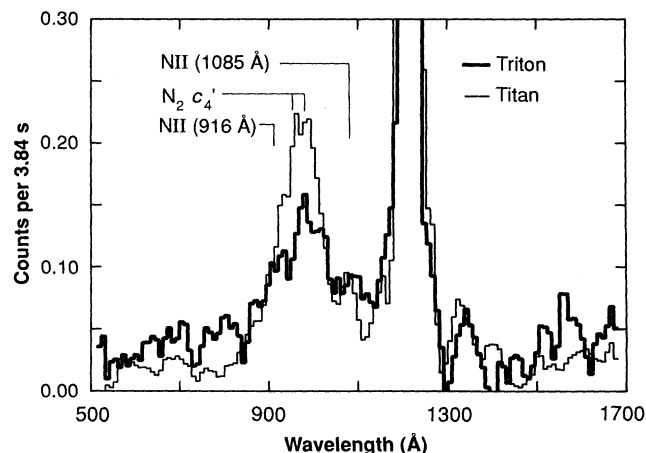


Fig. 6. Formation of two torus segments (plasma arcs) in Neptune's plasma equator. The plasma equatorial plane, shown here tilted approximately 40° to the spin equator, rotates with Neptune while Triton's orbit, tilted 21°, does not. Ionized gas from Triton intersects the plasma equator in two regions constrained to lie between the two latitude limits determined by the tilt of Triton's orbit. One plasma arc is estimated to lie in the longitude range 140° to 210°W and the other in the range 310° to 25°W. Gas escaping from Triton's atmosphere is preferentially ionized by enhanced electron impact as it crosses the plasma equator at the marked interaction regions. These interaction regions move along the plasma arcs with a 16.1-hour period.

Fig. 7. Disk-averaged spectra from the day sides of Triton and Titan. The heavy line shows the spectrum of Triton (integration time, 5690 s). On average, approximately 70% of the slit is filled by atmospheric emission. The light line shows the Titan spectrum obtained by Voyager 1 (integration time, 7246 s) (16) normalized to the Triton spectrum in the 1085 Å region.



dimmer by at least a factor of 2, except for the H Lyman α line, which has an intensity of 110 R on the day side and an upper limit of 90 R from the night side. This day/night asymmetry was also present in the atmosphere of Titan. Furthermore, the spectral shape is similar to that of Titan and presents some of the same puzzles. In particular, significant emission in the N_2 c'_4 (0,1) band is required to fit the peak near 970 Å, although these emissions are weak in the terrestrial dayglow (16).

Photoelectrons, solar fluorescence, and magnetospheric precipitation may contribute to the excitation of the airglow emissions. It is unlikely that solar fluorescence is responsible for the c'_4 bands, although it may contribute at other wavelengths (17). Photoelectrons may help explain the observed day/night asymmetry. We estimate an upper limit of 2 R for photoelectron-excited c'_4 emissions (18). The inferred intensity of the NII 1085 Å feature is larger than the value obtained by scaling the terrestrial intensity (19). This may indicate an additional excitation source, such as precipitation of the magnetospheric electrons detected by the low-energy charged particles experiment (20). Further spectral analysis is required for a quantitative estimate of the potential excitation sources and their relation to the ionosphere and thermal structure.

Occultations. Occultations of the sun and of β Canis Majoris by Triton complement each other and the airglow observations. At

the highest altitudes, transmission spectra from the solar occultation show a sharp onset of absorption below 800 Å. This absorption signature is characteristic of N₂ and Ar, with N₂ the likeliest candidate because of the EUV spectrum. Figure 8 shows light curves in this wavelength range from the solar entrance and exit occultations. The altitude scale is determined by the light curves at longer wavelengths that appear to have probed the atmosphere to the surface (21). These data allow determination of the temperature (if we assume hydrostatic equilibrium) and density variation of N₂ over the altitude range 500 to 700 km (10⁻⁶ to 10⁻⁵ μbar). The observed density variation is consistent with an isothermal atmosphere at 95 ± 5 K. The [CO]/[N₂] ratio is limited to ≤1% by the absence of extinction in the CO ionization continuum between 800 and 885 Å. At much lower altitudes the absorption signature of CH₄ is evident in the region from 800 to 1350 Å in both the solar and the β Canis Majoris occultations. We infer a CH₄ density in the summer hemisphere from the solar egress of ~10⁸ cm⁻³ at an altitude of 40 km with a density scale height of 7 to 10 km. Finally, absorption in the region from 1350 to 1700 Å is observed in the bottom scale height of the atmosphere. Neither N₂ nor CH₄ absorbs in this wavelength region, and the abundance of other potential absorbers should be negligible (22); therefore, it seems likely that this extinction is due to aerosols.

The CH₄ concentration shows pronounced latitudinal variations. Comparison of the solar ingress (winter) and egress (summer) light curves shows that the CH₄ concentration at 40 km in the winter hemisphere is greater by roughly a factor of 10 than in the summer. In addition, the CH₄ scale height at the solar ingress is 10 to 40% larger than the scale heights derived from the stellar light curves or the solar egress. These differences may be signatures of seasonal transport processes or variations in photochemistry. In contrast to the CH₄ distribution, the temperatures and densities above 500 km derived from the N₂ extinction show no seasonal asymmetry.

To examine the energetics of Triton's atmosphere and to estimate physical conditions in the lower atmosphere, we have constructed thermal models for Triton (23). The results are shown in Fig. 9. The model assumes that heat deposited in the upper atmosphere is carried downward by conduction to the tropopause and then from the tropopause to the surface by convection. The number densities and temperatures in the upper atmosphere are fixed by the UVS measurements. By solving the coupled hydrostatic and energy balance equations, we

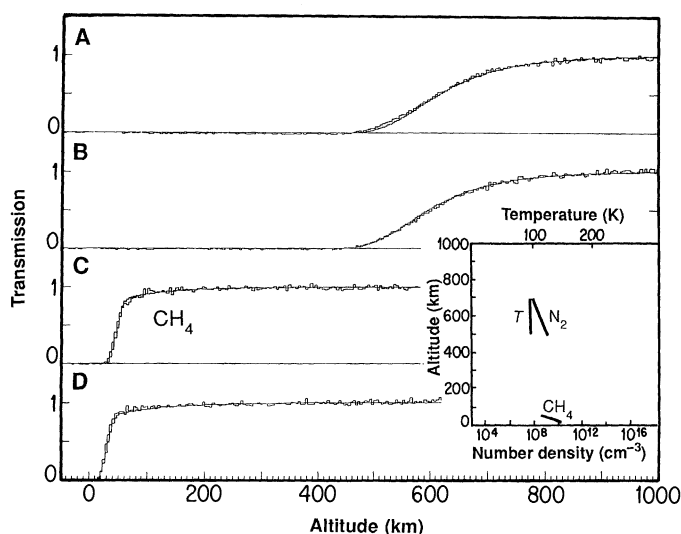


Fig. 8. Triton solar occultation. (A and B) Ingress and egress light curves at short wavelengths (569 < λ < 634 Å), where extinction is due to the N₂ ionization continuum. The solid lines show the transmission calculated from models with a temperature of 95 K above 400 km. (C and D) Ingress and egress curves at longer wavelengths (1171 < λ < 1236 Å), where CH₄ is the dominant absorber. In the models used to compute the solid lines, the CH₄ scale heights are 9.5 km (ingress) and 8.5 km (egress). The inset

shows measured number densities and temperatures. The CH₄ abundance is shown for the entrance occultation.

can extrapolate these number densities and temperatures to the lower atmosphere. The height of the tropopause was assumed to be 9 km. The temperature profile is consistent with the truncation of the haze layers and plumes seen in the imaging experiment (24), if the truncation corresponds to the change in static stability expected at the tropopause. A downward heat flux of 0.0016 erg cm⁻² s⁻¹ is required in this model to reproduce the 95 K exospheric temperature and a surface temperature near 38 K (8). The heat appears to be deposited near 400 km, which is close to the ionospheric peak (25). Above 400 km the atmosphere is isothermal. Below 9 km an adiabatic lapse rate of 0.1 K km⁻¹ is assumed. This thermal profile predicts a surface pressure of 14 μbar, which corresponds to the vapor pressure of nitrogen at 37.5 K, only marginally different from the model value. Thus, the atmosphere may be in vapor-pressure equilibrium with solid nitrogen. In our opinion the model is also consistent with the radio science results: we calculate that the density profiles shown here produce phase shifts within 0.2 radians of the radio measurements at all relevant altitudes (25).

A surface temperature of 38 to 39 K is consistent with expectations based on models of seasonal transport of N₂. The N₂ vapor pressure of ~14 μbar is large enough for latent heat effects to dominate the energetics of volatile transport. This is the basis for the conceptual model of volatile transport developed for Mars by Leighton and Murray (26) and first applied to a CH₄-dominated polar cap on Triton by Trafton (27). For cap albedos from 0.8 to 0.9 and an emissivity of ~0.5, we find a surface temperature of 34 to 40 K for an isothermal

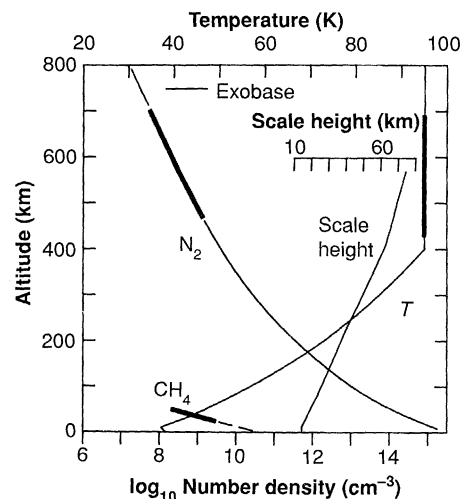


Fig. 9. Model of Triton's atmosphere fitted to the measured concentrations and temperature (heavy line portions). Temperatures, shown at right, were obtained empirically over the 450- to 700-km range and extended downward by a conduction model, on the assumption of a heat source of 1.6×10^{-3} erg cm⁻² s⁻¹ concentrated in a thin layer at 400 km. Sudden changes in slope in the profiles of temperature and scale height are due to this simplifying assumption. If there is a troposphere below 9 km, the temperature could break away as sketched. The variation of gravity with height has a major effect on the scale heights.

polar cap in saturation equilibrium with the atmosphere.

In contrast to N₂, the abundance of CH₄ appears to be far below saturation. The CH₄ mole fraction at 40 km is 2.5×10^{-6} , which is smaller by roughly a factor of 30 than the value expected if the CH₄ concentration in the upper atmosphere were controlled by the temperature at the tropopause. Also, the CH₄ scale height of ~7 to 10 km is far too small to be interpreted in terms of a tem-

perature in a hydrostatic distribution. Extrapolating to the surface implies that CH₄ is subsaturated by roughly a factor of 10. The small scale height at 40 km may be a photochemical effect. For this to occur, the rate of vertical mixing must be small. We estimate an eddy coefficient on the order of 10³ to 10⁴ cm² s⁻¹. An alternate explanation is that the CH₄ distribution is vapor pressure-controlled, with the small scale height caused by a negative temperature gradient. An adiabatic lapse rate at 40 km predicts CH₄ scale heights in accord with the data, but this model implies a temperature of ~32 K near 40 km, which is inconsistent with the radio science results. Therefore, we favor the photochemical explanation.

Because of the low CH₄ abundance and the weak vertical mixing, photochemistry on Triton will occur predominantly in the bottom 2 to 3 scale heights of the atmosphere. The principal products of photochemistry should be N, H₂, H, and C₂ hydrocarbons. Photolysis of CH₄ most often produces H₂ and CH₂, and the CH₂ may produce C₂H₆, C₂H₄, and C₂H₂. Because the atmosphere is so cold, the heavier hydrocarbons condense without further reaction, while the hydrogen escapes. Photolysis is driven by the solar and LISM H Lyman α line with a global mean flux of approximately 2 × 10⁸ photons cm⁻² s⁻¹, and this is also the rate of production of H₂ and CH₂. The flux of C₂ hydrocarbons to the surface is half as great and over 4.5 × 10⁹ years would give roughly 600 g cm⁻², the equivalent of a 6-m layer.

The H₂ created by photochemistry eventually escapes into the magnetosphere of Neptune. Escape of H₂ is diffusion-limited and is proportional to its mixing ratio *f*, which we estimate to be 100 ppm (28) in the lower atmosphere. In view of the nature of diffusion-limited flow, this value would pertain well above the homopause, in spite of the tendency toward diffusive separation. The diffusion-limited escape flux is ~2 × 10⁸ cm⁻² s⁻¹. If thermal escape is the dominant loss process, the hydrogen mixing ratio at the exobase, including both H and H₂, is roughly 200 ppm. The supply rate to the magnetosphere is approximately 10²⁵ atoms s⁻¹. The thermal escape flux of N₂ is a negligible 75 molecules cm⁻² s⁻¹; that of N depends on its unknown mixing ratio. Because the N₂ thermal escape rate is so low, nonthermal processes such as dissociative recombination or ion loss must dominate, if this source is to supply the 1 kg s⁻¹ needed for the Neptunian aurora (15).

There are several opportunities for further analysis. The N₂ densities can be measured to much lower altitudes by use of the electronic bands in the 1000 Å region. Much better information about the atmosphere

near the surface can be derived by a joint analysis of data from other experiments, notably the radio occultation and the plumes found in the images.

Neutrals and ions in Neptune's system. A preliminary search for extended emissions from ions and neutrals near Triton and in its orbit yielded upper limits of ~5 R except for H Lyman α. If electron impact excitation is the dominant process, the number densities must be less than 10⁵ N cm⁻³ (1135 Å), 3 × 10⁵ N⁺ cm⁻³ (916 Å), and 10⁸ N₂ cm⁻³ (960 Å), in a 10-R_N column if we assume an electron gas with a density of 0.1 cm⁻³ and a temperature of 10,000 K. The occultation experiment constrains the N and N₂ number density above the atmosphere to 10⁷ cm⁻³ or less, averaged over a 2-R_N column. The search for H Lyman α emission from the system is hampered by the large LISM background.

Rings. In addition to the atmospheric occultations described here, the UVS also observed an occultation of the B2.5 V star σ Sagittarii by the ring system. This occultation (Table 1), which was simultaneously observed by the photopolarimeter experiment (29), intersected the ring plane between 3.1 and 1.7 R_N. The only event unambiguously identified in the UVS data is associated with NIR. This event appears as a low τ feature (⟨τ⟩ = 0.02) having a total width of approximately 35 km with a somewhat more opaque central core ~15 km wide. The equivalent width, defined as the width-integrated optical depth of the ring, was found to be 0.66 ± 0.12 km. The absorption feature caused by the ring is centered at spacecraft event time 236/23:24:46.37, which corresponds to a planetocentric radius of 62,843 km for the ring, assuming a Neptune rotation pole of right ascension α = 298.9° and declination δ = 42.8°

REFERENCES AND NOTES

1. The UV albedo and its relation to the IR measurements is discussed by J. J. Caldwell *et al.*, *Icarus* **74**, 133 (1988); for H Lyman α, see J. T. Clarke, *Geophys. Res. Lett.* **15**, 701 (1988); for hydrocarbons, see G. S. Orton *et al.*, *Icarus* **70**, 1 (1987); for stellar occultations, see R. G. French *et al.*, *ibid.* **55**, 332 (1983); for solid CH₄ and N₂, see D. P. Cruikshank, *Science* **245**, 283 (1989).
2. The UVS covers the wavelength range of approximately 500 to 1700 Å with 126 contiguous channels and has a field of view of 0.1° by 0.86°. Its design and operation have been described by A. L. Broadfoot *et al.* [*Space Sci. Rev.* **21**, 183 (1977); *J. Geophys. Res.* **86**, 8259 (1981)].
3. In the analysis of these observations, we have followed the procedure described by F. Herbert *et al.*, *J. Geophys. Res.* **92**, 15093 (1987).
4. The effect of gas drag on the lifetimes of ring particles has been discussed by A. L. Broadfoot *et al.*, *Science* **233**, 74 (1986) and Herbert *et al.* (3). With the 750 K thermospheric temperature, the atomic H number density is approximated by n_H (cm⁻³) = 3 × 10⁻¹⁰ exp(40/*r*) with the radius *r* in

units of R_N. If we use the formulas of Herbert *et al.*, the time (*t* in years) required for the orbit of size *r* of a ring particle of radius *a* (in centimeters) to decay to the planetary surface solely under the influence of gas drag is given by $t(r) = 2.5 \times 10^{18} a^{3/2} \exp(-40/r)$. At *r* = 1.6, for example, $t = 7 \times 10^7$ years for a 1-cm ring particle. Inward from this, the decay times decrease rapidly with declining orbital radius. However at *r* = 2.5, the decay time is longer than the age of the solar system for particles larger than a few tens of micrometers in size.

5. B. J. Conrath *et al.*, *Science* **246**, 1454 (1989).
6. P. N. Romani and S. K. Atreya, *Geophys. Res. Lett.* **16**, 941 (1989).
7. R. V. Yelle, J. C. McConnell, D. F. Strobel, L. R. Doose, *Icarus* **77**, 439 (1989).
8. R. V. Yelle *et al.*, *J. Geophys. Res.* **92**, 15110 (1987).
9. Voyager encountered Jupiter, Saturn, and Neptune at times of high solar activity, but the Uranus encounter was at solar minimum. No adjustment for solar cycle effects has been included in the scaling of the spectra.
10. R. V. Yelle, L. R. Doose, M. G. Tomasko, D. F. Strobel, *Geophys. Res. Lett.* **14**, 483 (1987).
11. R. V. Yelle, *ibid.* **15**, 1145 (1988).
12. M. R. Torr and D. G. Torr, *J. Geophys. Res.* **90**, 6675 (1985).
13. The analyses appear in (Jupiter) J. C. McConnell *et al.*, *Planet. Space Sci.* **29**, 283 (1981); (Saturn) B. R. Sandel *et al.*, *Geophys. Res. Lett.* **9**, 1077 (1982); *Science* **215**, 548 (1982); Herbert *et al.* (3). The value of *K* given in the text for Saturn has been roughly adjusted for a more recent value (3% instead of 6%) of the helium mole fraction [B. J. Conrath *et al.*, *Astrophys. J.* **282**, 807 (1984)].
14. The current is $J = (1 + 3/2f^2)\sigma\Omega^2r/B$, where σ is the axial mass density, Ω is Neptune's angular velocity, *r* is the distance to the plasma arc, *B* is the local magnetic field strength, and *f* is the ratio of thermal speed to Ωr [A. J. Dessler, *Planet. Space Sci.* **28**, 781 (1980)]. We assume $f = 2/3$, and we choose $\sigma = 10^{-4}$ kg m⁻¹ in order to obtain a current $J = 2 \times 10^5$ A.
15. To achieve this power level from a centrifugally driven torus, A. J. Dessler [*Icarus* **44**, 291 (1980)] requires a mass input rate $dm/dt = 1$ kg s⁻¹ and an ancillary assumption that the arc plasma stays in effective corotation with Neptune out to 20 R_N. Such mass injection implies an N₂ escape flux from Triton of 10⁸ cm⁻² s⁻¹.
16. See D. F. Strobel and D. E. Shemansky, *J. Geophys. Res.* **87**, 1361 (1982) for a discussion of the Titan airglow spectrum and the *c*₄ bands.
17. The *c*₄ (0,0) band should absorb solar continuum radiation at 958 Å. For the model atmosphere used here we estimate an equivalent width of this band of 7.4 Å, implying a net intensity of only 0.1 R. At longer wavelengths the strong solar CIII 977 Å and H Lyman γ lines are absorbed by the b¹Π_u (3,0)_u band but this state predissociates strongly and should not contribute to the emissions.
18. The column production rate of photoelectrons capable of exciting the *c*₄ state is approximately 6 × 10⁷ cm⁻² s⁻¹ [H. S. Ogawa and D. L. Judge, *J. Geophys. Res.* **91**, 7089 (1986)] and the efficiency for exciting the *c*₄ state is ~3% [J. L. Fox and G. A. Victor, *Planet. Space Sci.* **36**, 329 (1987)], yielding a column production rate of 2 × 10⁶ photons cm⁻² s⁻¹. If all of these photons escape the atmosphere, the implied intensity is 2 R.
19. S. Chakrabarti *et al.* [*J. Geophys. Res.* **88**, 4898 (1983)] reported an intensity of 500 R for the NII 1085 Å feature in the terrestrial dayglow near solar maximum. Scaling to Triton and dividing by the N₂ mole fraction at 150 km in the terrestrial atmosphere gives an intensity of 0.8 R.
20. S. M. Krimigis *et al.*, *Science* **246**, 1483 (1989).
21. This conclusion is based on a comparison of the relative timing of the ingress and egress events together with the manner in which the signals disappeared and reappeared. The observed occultation chord lengths, between the loss and reappearance of signal, are 2655 ± 10 km for the stellar and 2479 ± 6 km for the solar occultations. Respectively, these values are 42 and 11 km less than those predicted from spacecraft trajectory information. Both results are marginally consistent with a Triton

radius of 1350 ± 5 km (T. Johnson, personal communication) and a 1-s (~ 20 -km) uncertainty in the spacecraft trajectory. At the lowest atmospheric levels probed by the occultation, the signals do not go smoothly to zero but appear to cease abruptly, supporting our contention that the source has passed below the limb.

22. Because of the low temperatures, we expect that the abundance of other potential absorbers, such as C_2H_2 , C_2H_6 , and hydrogen cyanide (HCN), will be limited to negligible levels by their vapor pressures.
23. Use of this model for Triton was suggested to us by E. Lellouch. See E. Lellouch *et al.*, *Icarus*, in press.
24. B. A. Smith *et al.*, *Science* **246**, 1422 (1989).
25. G. L. Tyler *et al.*, *ibid.*, p. 1466.
26. R. B. Leighton and B. C. Murray, *Science* **153**, 136

- (1966).
27. L. M. Trafton, *Icarus* **58**, 293 (1984).
28. The mixing ratio is $f = QH/b$, where Q is the production rate, equal to the upward flux, H is the scale height at the homopause (20 km), and $b = 3.5 \times 10^{18} \text{ cm}^{-1} \text{ s}^{-1}$ is the product of diffusion coefficient and number density [D. M. Hunten, *J. Atmos. Sci.* **30**, 726 (1973)].
29. A. L. Lane *et al.*, *Science* **246**, 1450 (1989).
30. N. F. Ness *et al.*, *ibid.*, p. 1473.
31. We thank M. Summers for performing photochemical calculations and M. Stevens for thermal conduction calculations in support of this analysis. We thank J. Stansberry for aerosol production calculations and V. Eshleman for helpful discussions. We thank the Voyager Project personnel at the Jet

Propulsion Laboratory for their enthusiastic efforts that have made this mission successful. We acknowledge the work of the Voyager Spacecraft Team, particularly G. Hanover and H. Marderness, whose fine tuning of scan platform pointing and spacecraft stabilization led to exceptionally good occultation observations during this encounter. Supported by the Jet Propulsion Laboratory, California Institute of Technology, under National Aeronautics and Space Administration (NASA) contract NAS1-100. Additional support was provided by the Planetary Sciences Discipline of NASA's Office of Space Sciences.

31 October 1989; accepted 15 November 1989

Voyager Radio Science Observations of Neptune and Triton

G. L. TYLER, D. N. SWEETNAM, J. D. ANDERSON, S. E. BORUTZKI, J. K. CAMPBELL, V. R. ESHLEMAN, D. L. GRESH, E. M. GURROLA, D. P. HINSON, N. KAWASHIMA, E. R. KURSINSKI, G. S. LEVY, G. F. LINDAL, J. R. LYONS, E. A. MAROUF, P. A. ROSEN, R. A. SIMPSON, G. E. WOOD

The Voyager 2 encounter with the Neptune system included radio science investigations of the masses and densities of Neptune and Triton, the low-order gravitational harmonics of Neptune, the vertical structures of the atmospheres and ionospheres of Neptune and Triton, the composition of the atmosphere of Neptune, and characteristics of ring material. Demanding experimental requirements were met successfully, and study of the large store of collected data has begun. The initial search of the data revealed no detectable effects of ring material with optical depth $\tau \approx 0.01$. Preliminary representative results include the following: 1.0243×10^{26} and 2.141×10^{22} kilograms for the masses of Neptune and Triton; 1640 and 2054 kilograms per cubic meter for their respective densities; 1355 ± 7 kilometers, provisionally, for the radius of Triton; and $J_2 = 3411 \pm 10 (\times 10^{-6})$ and $J_4 = -26^{+12}_{-20} (\times 10^{-6})$ for Neptune's gravity field (J_2 and J_4 are harmonic coefficients of the gravity field). The equatorial and polar radii of Neptune are $24,764 \pm 20$ and $24,340 \pm 30$ kilometers, respectively, at the 10^5 -pascal (1 bar) pressure level. Neptune's atmosphere was probed to a pressure level of about 5×10^5 pascals, and effects of a methane cloud region and probable ammonia absorption below the cloud are evident in the data. Results for the mixing ratios of helium and ammonia are still being investigated; the methane abundance below the clouds is at least 1 percent by volume. Derived temperature-pressure profiles to 1.2×10^5 pascals and 78 kelvins (K) show a lapse rate corresponding to "frozen" equilibrium of the para- and ortho-hydrogen states. Neptune's ionosphere exhibits an extended topside at a temperature of 950 ± 160 K if H^+ is the dominant ion, and narrow ionization layers of the type previously seen at the other three giant planets. Triton has a dense ionosphere with a peak electron concentration of 46×10^9 per cubic meter at an altitude of 340 kilometers measured during occultation egress. Its topside plasma temperature is about 80 ± 16 K if N_2^+ is the principal ion. The tenuous neutral atmosphere of Triton produced distinct signatures in the occultation data; however, the accuracy of the measurements is limited by uncertainties in the frequency of the spacecraft reference oscillator. Preliminary values for the surface pressure of 1.6 ± 0.3 pascals and an equivalent isothermal temperature of 48 ± 5 K are suggested, on the assumption that molecular nitrogen dominates the atmosphere. The radio data may be showing the effects of a thermal inversion near the surface; this and other evidence imply that the Triton atmosphere is controlled by vapor-pressure equilibrium with surface ices, at a temperature of 38 K and a methane mixing ratio of about 10^{-4} .

VOYAGER RADIO SCIENCE (RSS) observations of the Neptune system comprise coherent radio Doppler and ranging measurements for the study of

Neptune's gravity and the mass of Triton, radio occultation measurements of the atmosphere of Neptune and Triton, and a radio occultation search for Neptune's ring

arcs. Experimental and analytical techniques are similar to those used previously (1, 2), with the exception that for Triton the technique of diffraction correction developed for the study of planetary rings was extended for the first time to the study of atmospheres.

The occultation experiments are based on the geometry obtained as Voyager passed behind Neptune and Triton (Fig. 1). Unmodulated, dual-frequency transmissions at wavelengths of 3.6 and 13 cm from Voyager's telecommunication transmitters (3) were used to probe the intervening atmosphere and possible ring material. These signals were received simultaneously at three tracking stations: the 70-m (diameter) antenna of the National Aeronautics and Space Administration (NASA) Deep Space Network at Tidbinbilla, Australia, received both wavelengths, while the 64-m Commonwealth Scientific and Industrial Research Organization (CSIRO) antenna at Parkes, Australia, received only the 3.6-cm signal, and the 64-m Institute of Space and Astronautical Science antenna at Usuda, Japan, received only the 13-cm signal. Provisions were made for coherent arraying of the stations during future data reduction for the purpose of improving the signal-to-noise ratio (4).

We report here preliminary results for the gravity field of Neptune, the mass and density of Triton, the ionosphere and atmosphere of Neptune, and the ionosphere and atmosphere of Triton, including a measurement of the surface pressure of Triton. These initial results are based on a combination of data from the real-time tracking and monitoring systems used in collecting the data (5) and from a limited analysis of the primary data from the Tidbinbilla station (6). Nep-

G. L. Tyler, V. R. Eshleman, D. L. Gresh, E. M. Gurrola, D. P. Hinson, E. A. Marouf, P. A. Rosen, R. A. Simpson, Stanford University, Stanford, CA 94305.
D. N. Sweetnam, J. D. Anderson, S. E. Borutzki, J. K. Campbell, E. R. Kursinski, G. S. Levy, G. F. Lindal, J. R. Lyons, G. E. Wood, Jet Propulsion Laboratory, California Institute of Technology, Pasadena, CA 91109.
N. Kawashima, Institute of Space and Astronautical Science, Sagami-hara, 229 Japan.